Journal of the European Ceramic Society 38 (2018) 3104–3110

Contents lists available at ScienceDirect

Journal of the European Ceramic Society

journal homepage: www.elsevier.com/locate/jeurceramsoc

Original article

Electric field induced phase transition and accompanying giant poling strain in lead-free $NaNbO_3$-$BaZrO_3$ ceramics

Mengxian Dou, Jian Fu, Ruzhong Zuo*

Institute of Electro Ceramics & Devices, School of Materials Science and Engineering, Hefei University of Technology, Hefei, 230009, PR China

ARTICLE INFO

Keywords:
Lead-free ceramics
Phase transition
Antiferroelectric
Ferroelectric
Strains

ABSTRACT

A series of phase transitions in (1-x)$NaNbO_3$-x$BaZrO_3$ ((1-x)NN-xBZ) ceramics was observed from antiferroelectric orthorhombic phase to ferroelectric orthorhombic phase and finally into ferroelectric rhombohedral phase with increasing x. An electric field induced irreversible phase transition was found in different compositions, irrespective of their virgin phase structures. Particularly, an antiferroelectric orthorhombic phase is irreversibly transformed into a ferroelectric monoclinic phase within $0.02 \le x \le 0.05$, leading to a giant poling strain of ~0.58%. This is much larger than that observed in ferroelectric orthorhombic ($0.06 \le x \le 0.07$) and rhombohedral phases ($0.08 \le x \le 0.11$) suffering from an irreversible ferroelectric-ferroelectric (monoclinic) phase transition. The synchrotron x-ray diffraction and the measurement of longitudinal and transverse strains suggest that this irreversible phase transition should involve not only a distinct volume expansion, but also an obvious lattice elongation. The present study demonstrates a unique nature of the composition and field dependent phase stability and an underlying mechanism of giant poling strains in NN-BZ ceramics.

1. Introduction

Increasing attention has recently been focused on developing lead-free ferroelectric materials with large strains for actuator applications. The typical $NaNbO_3$-$KNbO_3$ (NN-KN) based phase-boundary compositions were reported to exhibit strain values of 0.1–0.2% [1–3], as a result of the coupling of converse piezoelectric effect and domain switching. Large strains of up to 0.31% have been recently reported in modified NKN based piezoelectric ceramics by introducing a normal ferroelectric-weak relaxor ferroelectric phase transformation [4].

NN is a typical lead-free antiferroelectric material at room temperature, and exhibits a complex phase structure change involving the tilting of the oxygen octahedron and the displacement of the Nb^{5+} ion from its octahedral center [5–7]. As known, $PbZrO_3$-based antiferroelectric ceramics usually exhibit large strains owing to electric-field induced antiferroelectric tetragonal-ferroelectric rhombohedral phase transition, accompanying a distinct increase in the unit cell volume [8]. It is thus reasonable to expect high strain values in NN-based antiferroelectric ceramics. The room-temperature crystal structure of NN was considered to be an antiferroelectric orthorhombic phase with the space group Pbma ($a \approx 5.56$, $b \approx 15.3$ and $c \approx 5.50$ Å) [6,9], although a weak ferroelectricity was also found at room temperature in terms of the complicated features of polarization versus electric field ((P−E)) hysteresis loops [10,11]. The detailed structure analysis has indicated that the antiferroelectric orthorhombic P phase may coexist with ferroelectric orthorhombic Q (with space group $P2_1ma$) phase in a variety of ways due to their comparable free energy [12–16]. Several studies have been carried out on stabilizing the antiferroelectric phase in NN-based ceramics in recent years [17–19]. Unfortunately, the strain values achieved so far in these NN-based antiferroelectric ceramics are only 0.2–0.3% [10,20].

In this work, (1-x)NN-x$BaZrO_3$ ((1-x)NN-xBZ) binary solid solution ceramics were prepared, in which BZ was used to stabilize the ferroelectric phase. A giant poling strain of up to 0.58% was generated in NN-BZ compositions and found to be closely related with an electric field induced irreversible phase transition, as evidenced by in-situ synchrotron X-ray diffraction (XRD) and the longitudinal and transverse strain measurement.

2. Experimental

The (1-x)NN-xBZ ceramics were prepared by a conventional solid-state reaction method using high-purity (> 99%) Na_2CO_3, Nb_2O_5, $BaCO_3$ and ZrO_2 as raw-materials. The starting powders were weighed according to the stoichiometric formula and ball-milled for 8 h in ethanol with zirconia balls. The dried powders were calcined at 750 °C for 2 h and then calcined at 850–900 °C for 3 h. After calcination, the powders were ball milled again for 10 h. The powders were pressed into

* Corresponding author.
E-mail address: piezolab@hfut.edu.cn (R. Zuo).

https://doi.org/10.1016/j.jeurceramsoc.2018.03.008
Received 11 December 2017; Received in revised form 13 February 2018; Accepted 7 March 2018
Available online 08 March 2018
0955-2219/

pellets with 10 mm in diameter and then sintered in sealed crucibles at 1345–1370 °C for 2 h.

The crystal structure was examined by an X-ray diffractometer (XRD, D/Max-RB, Rigaku, Tokyo, Japan) using Cu Ka radiation. To quantitatively describe the phase structure, the XRD data were analyzed by the Rietveld refinement using GSAS software. The microstructure of the polished and thermally-etched specimens was observed using a field-emission scanning electron microscope (FE-SEM, JEOL JSM-6490LV, Tokyo, Japan). The as-sintered ceramics were ground and polished, and then annealed at 500 °C for 4 (h) to remove mechanical stress. Silver paste was painted on major sides of the polished samples and then fired at 550 °C for 30 min. Dielectric properties were measured as a function of temperature and frequency by an LCR meter (Agilent E4980A, Santa Clara, CA) in the frequency range of 1 kHz–1 MHz in the temperature range of 30–500 °C. The P-E hysteresis loops and electric field versus strain (S-E) curves as a function of composition were measured simultaneously by using a ferroelectric measuring system (Precision multiferroelectric, Radiant Technologies Inc., Albuquerque, NM) with an accessory laser interferometer vibrometer (AE SP-S 120E, SIOS Mebtechnik, GmbH, Ilmenau, Germany).

For in-situ synchrotron XRD measurement, thin gold electrodes were sputtered onto two well-polished sides of the ceramic disks. The in-situ XRD measurements were carried out at beamline 14B1 (λ = 1.2398 Å) at Shanghai Synchrotron Radiation Facility (SSRF) through θ–2θ step-scans using a Huber 5021 six-circle diffractometer with a NaI scintillation detector.

3. Results and discussion

Fig. 1(a) shows the XRD patterns of (1-x)NN-xBZ ceramics at room temperature. All compositions exhibit a pure perovskite structure without any secondary phases. It can be found that the diffraction peaks shift to lower angles with increasing the BZ content, indicating that there is a slight lattice expansion probably owing to the relatively large ionic radii of Ba^{2+} and Zr^{4+} (CN = 12, R_{Ba} = 1.61 Å, R_{Na} = 1.39 Å; CN = 6, R_{Zr} = 0.72 Å, R_{Nb} = 0.64 Å) [21]. In addition, the addition of BZ is found to induce an obvious change of the crystal symmetry. As shown in Fig. 1(b) and (c), distinct superlattice peaks denoted as {11} and {21} can be observed in pure NN (x = 0), which are the typical feature of the antiferroelectric orthorhombic P phase of NN (JCPDS #33-1270). With the substitution of BZ for NN, both superlattice peaks decrease in intensities monotonously and cannot be detected as x ≥ 0.06. Instead, obvious features of the ferroelectric orthorhombic Q phase (JCPDS #82-0606) can be observed in the composition range of 0.06 ≤ x ≤ 0.07, indicating the occurrence of the phase transition from the antiferroelectric orthorhombic P phase to the ferroelectric orthorhombic Q phase. However, it can be seen from Fig. 1(d) that the split (200) pseudo-cubic diffraction peaks around 45° due to the ferroelectric orthorhombic distortion merge gradually into a single one as x ≥ 0.08. This phenomenon should result from the ferroelectric orthorhombic to rhombohedral phase transition.

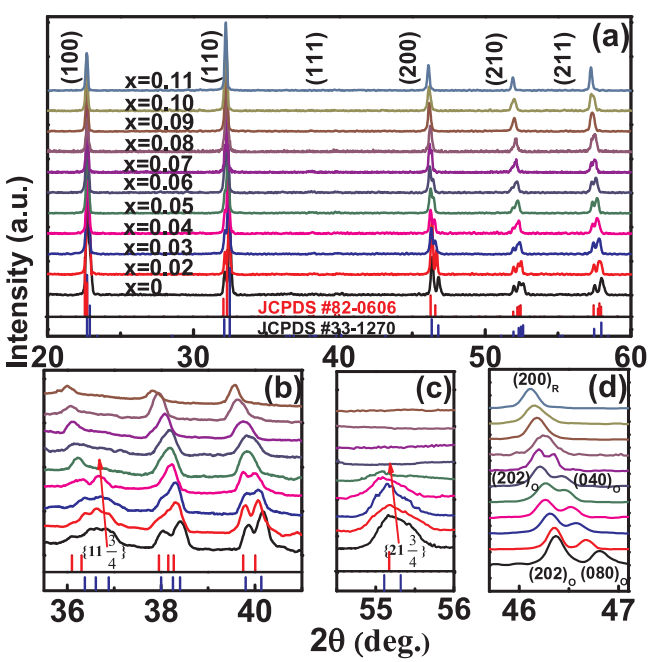

Fig. 1. (a) XRD patterns of (1-x)NN-xBZ ceramics, close view of (b) {11} and (c) {21} antiferroelectric superlattice peaks, and (d) pseudo-cubic (200) peaks changing with x.

In order to quantitatively investigate the observed antiferroelectric P phase, ferroelectric orthorhombic Q phase and ferroelectric rhombohedral phase, the Rietveld analysis of the XRD data using the GSAS software was carried out. According to the Glazer's structural description [22], the antiferroelectric P phase has pairs of alternating layers with $a^-b^+a^-$ and $a^-b^-a^-$ oxygen octahedral tilting, however, for the ferroelectric Q and rhombohedral phases, oxygen octahedral tilting can be described as $a^-b^+c^-$ and $a^-a^-a^-$, respectively. This suggests that P, Q and rhombohedral phases can be well described by Pbma, $P2_1ma$ and R3c space groups, respectively [23]. Fig. 2 depicts the observed, calculated, and difference profiles after the Rietveld analysis of the full XRD patterns for the selected compositions using these three space groups. It can be seen that the overall fit between the observed and calculated profiles is very good for all samples. The results of the Rietveld refinement are given in Table 1. The ferroelectric orthorhombic Q phase can be observed even at x = 0 sample. With increasing BZ content, the fraction of the Q phase decreases monotonously, and only Q phase can be observed at x = 0.07. With further increasing BZ content, the ferroelectric rhombohedral R3c phase can be detected at x > 0.07 and becomes dominant as x ≥ 0.10.

Fig. 3 shows the SEM micrographs of the polished and thermally etched (1-x)NN-xBZ ceramics sintered at their optimum temperatures. The results indicate that all the samples have high densities and well-developed grains. Moreover, it can be seen that the change of the BZ content has only a slight effect on the grain size and morphology of (1-x)NN-xBZ ceramics. The polygonal grains own an average size of ~8 μm.

The dielectric permittivity ε_r as a function of temperature and frequency for both unpoled and poled (1-x)NN-xBZ ceramics is shown in Figs. 4(a–g). In pure NN ceramic, there is a clear dielectric peak T_1 around 350 °C as a result of the structure phase transition from the

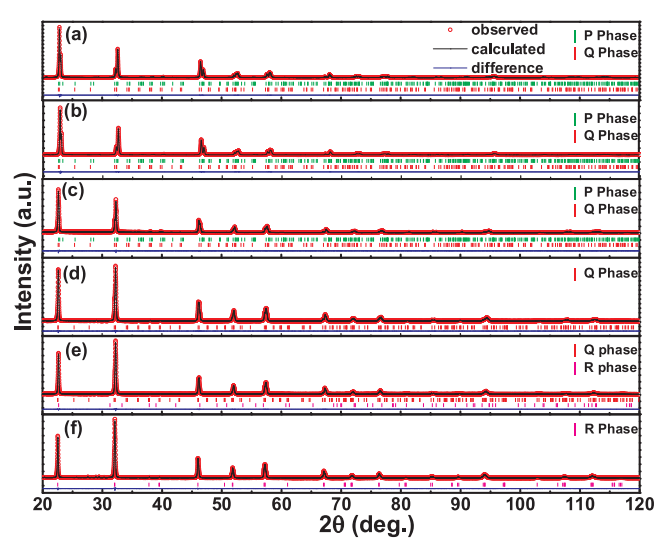

Fig. 2. Rietveld refinement plots of a few selected (1-x)NN-xBZ ceramics: (a) x = 0, (b) x = 0.02, (c) x = 0.05, (d) x = 0.07, (e) x = 0.08 and (f) x = 0.10.

Table 1
Refined structural parameters by using the Rietveld method for a few selected (1-x)NN-xBZ ceramics.

x	Space group	Lattice parameters	V (Å^3)	Fraction (%)	R_{wp} (%)	R_p (%)	χ^2
0	Pbma	a = 5.5697(6) Å, b = 15.5227(9) (Å), c = 5.5032(8) (Å), α = 90°, β = 90°, γ = 90°	475.8	90	8.82	6.85	2.77
	$P2_1ma$	a = 5.5748(2) Å, b = 7.7868(2) (Å), c = 5.5162(2) (Å), α = 90°, β = 90°, γ = 90°	239.4	10			
0.02	Pbma	a = 5.5603(8) Å, b = 15.5510(2)(9) (Å), c = 5.5060(3) (Å), α = 90°, β = 90°, γ = 90°	476.1	63	9.42	7.21	2.82
	$P2_1ma$	a = 5.5764(3) Å, b = 7.7903(1) (Å), c = 5.5174(6) (Å), α = 90°, β = 90°, γ = 90°	239.6	37			
0.05	Pbma	a = 5.5580(8) Å, b = 15.6583(3) (Å), c = 5.5082(1) (Å), α = 90°, β = 90°, γ = 90°	477.2	24	9.53	7.27	2.86
	$P2_1ma$	a = 5.7178(7) Å, b = 7.7743(7) (Å), c = 5.4765(8) (Å), α = 90°, β = 90°, γ = 90°	241.4	76			
0.07	$P2_1ma$	a = 5.5855(1) Å, b = 7.8458(6) (Å), c = 5.5482(4) (Å), α = 90°, β = 90°, γ = 90°	243.1	100	7.81	6.07	2.28
0.08	$P2_1ma$	a = 5.5905(8) Å, b = 7.8646(3) (Å), c = 5.571(1) (Å), α = 90°, β = 90°, γ = 90°	244.3	72	7.45	5.82	2.39
	R3c	a = b = 5.7102(2) Å, c = 12.8041(8) Å	361.5	28			
0.10	R3c	a = b = 5.5671(2) Å, c = 13.6756(1) Å	367.1	100	7.3	5.5	2.42

antiferroelectric orthorhombic P phase to the antiferroelectric orthorhombic R phase [24,25]. The corresponding temperature at the T_1 peak is well known as T_c in NN. In addition, two extra dielectric anomalies (labeled as T_2 and T_3) above room temperature can be observed after the addition of BZ. On the one hand, the dielectric anomaly T_2 that is believed to originate from the antiferroelectric R phase to paraelectric S phase transition [7], is found to move downwards and finally to merge with the T_1 peak (T_c) as $x \geq 0.07$. On the other hand, the dielectric anomaly T_3 due to the ferroelectric-antiferroelectric phase transition can be clearly detected in the x = 0.05 virgin sample, compared with the $x < 0.05$ virgin samples. This is because the ferroelectric Q phase is dominated in the x = 0.05 sample, although the P phase with a Pbma symmetry and the Q phase with a $P2_1ma$ symmetry coexist in a wide composition range of x = 0–0.05 according to the XRD results. However, T_3 can be observed in the x = 0.02 sample only after poling, indicating that an external electric field can favor the stabilization of the ferroelectric phase and the ferroelectric phase should be dominated at $x \geq 0.02$. However, it is unclear whether or not the crystal structure of the electric field induced ferroelectric phase is the same as that of the ferroelectric Q phase at the virgin state. It can be seen from Fig. 4(b–d) that the temperature range of the antiferroelectric P phase ($T_3 < T < T_c$) is obviously compressed with increasing the BZ content, so that only ferroelectric Q phase can be maintained in the temperature range between room temperature and T_c as $x \geq 0.06$. In addition, it is worthy of note that there should exist a low-temperature dielectric anomaly corresponding to the ferroelectric rhombohedral to orthorhombic phase transition [22]. This anomaly peak appears between room temperature and −50 °C as $x \geq 0.02$ and moves close to room temperature with increasing x, thus inducing a ferroelectric rhombohedral to orthorhombic phase transition at $T_{R\text{-}O}$ as $x \geq 0.08$, as shown in Fig. 4((h)).

Fig. 5(a–e) shows the first and second cycles of bipolar S-E curves of a few typical (1-x)NN-xBZ compositions at room temperature. The first cycles were measured from the virgin samples, after which the second cycles were recorded. It is obvious from Fig. 5(f) that a giant poling strain S1 of ~0.43–0.58% can be observed in the x = 0.02–0.05 samples due to the existence of an antiferroelectric phase, which can be irreversibly transformed into a ferroelectric phase under the application of external fields. The monotonous decrease in S1 at x = 0.02–0.05 should be attributed to the decrease of the antiferroelectric phase fraction, as can be seen from Table 1. Once the antiferroelectric phase cannot be detected, the poling strain values show an obvious decrease approximately at x = 0.07. However, compared with single rhombohedral phase zone (only ~0.2% for $x \geq 0.10$), the ferroelectric orthorhombic and rhombohedral phase coexistence zone exhibits relatively high S1 values (0.3–0.35% for x = 0.07–0.09).

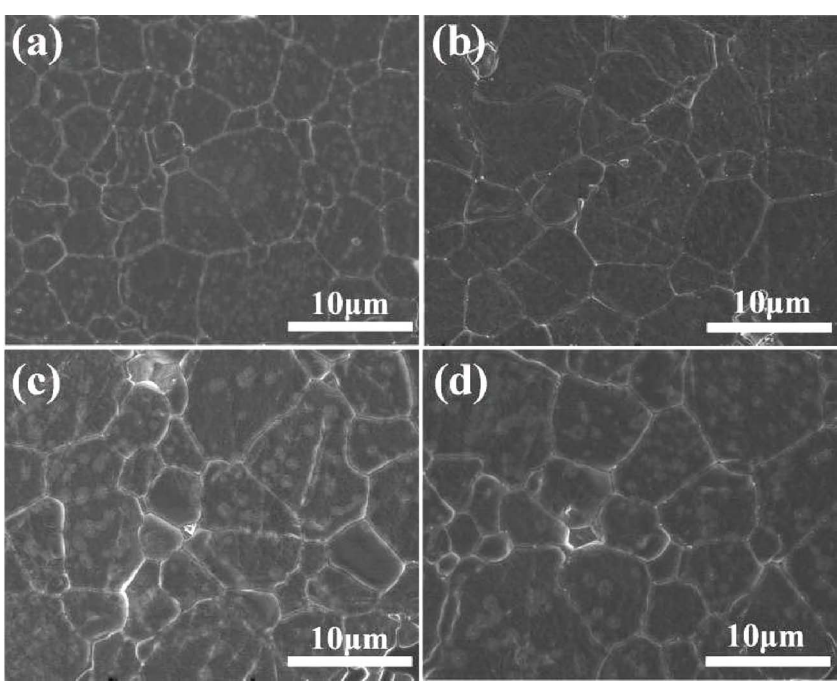

Fig. 3. SEM micrographs of (1-x)NN-xBZ ceramics sintered at their optimum temperatures: (a) x = 0.02, (b) x = 0.05, (c) x = 0.07 and (d) x = 0.10.

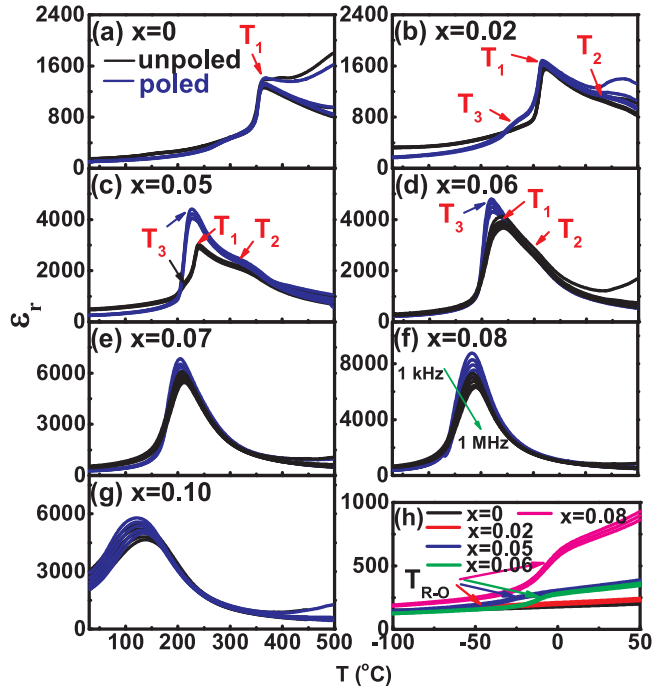

Fig. 4. (a–g) The dielectric permittivity as a function of temperature and frequency for both unpoled and poled (1-x)NN-xBZ ceramics from room temperature to 500 °C in the frequency range of 1 kHz–1 MHz, and (h) the dielectric permittivity as a function of temperature and frequency of unpoled (1-x)NN-xBZ ceramics from −100 °C to 50 °C.

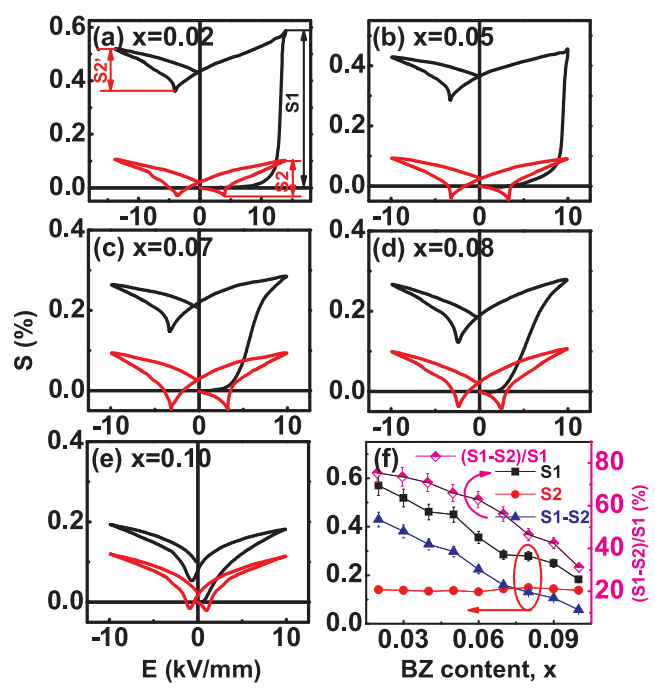

Fig. 5. (a–e) The first and second cycles of bipolar S-E curves of a few typical (1-x)NN-xBZ compositions at room temperature, and (f) composition-dependent first-cycle poling strain S1, second-cycle poling strain S2, and the irreversible strain S_{irr} (=S1–S2), and the irreversible contribution strain fraction in the total poling strain (S1–S2)/S1.

It is worthy of note that all samples exhibit asymmetric strain curves with a large strain gap. However, symmetric S-E curves with relatively small poling strains S2 were obtained after the first-cycle electric field loading. This indicates that all compositions exhibit an obvious field-induced irreversible phase transition. The strain gap can be thus termed as irrecoverable strain (S_{irr} = S1–S2). In addition, it can be seen from Fig. 5(f) that the poling strain S2 from electrically cycled samples

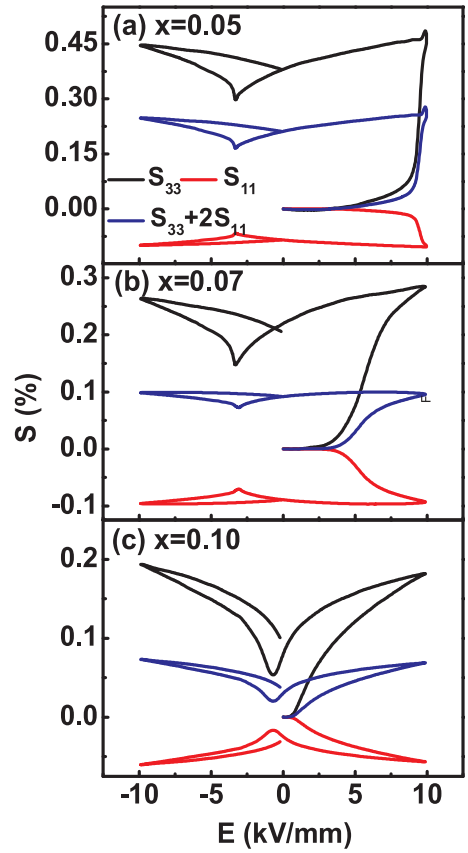

Fig. 6. The longitudinal S_{33}, transverse S_{11} strains and the corresponding volume change (S_{33} + $2S_{11}$) in response to extend electric fields for virgin samples with (a) x = 0.05, (b) x = 0.07, and (c) x = 0.10.

exhibits little composition-dependence and shows a good agreement with S2' values on the negative field side in the first cycle of each sample, suggesting that the field induced ferroelectric phase should be similar in the crystal symmetry and property in different compositions, as discussed in detail infra. S2 should be mainly attributed to the domain switching and piezoelectric effect of the electric field induced ferroelectric phase. Most importantly, it can be seen from Fig. 5(f) that in the antiferroelectric phase zone (x = 0.02–0.05), the strain contribution from the irreversible phase transition can reach up to 70–75%, as estimated by calculating the value of (S1–S2)/S1. By comparison, this value decreases down to 25-50% in the ferroelectric phase zone (0.06 ≤ x ≤ 0.11).

To reveal the origin of such high irreversible strains in the first cycle S-E curves, the electric field induced first-cycle longitudinal and transverse strains and the resulting volume change for a few selected compositions are shown in Fig. 6. It can be seen that the longitudinal strain expands distinctly, accompanied by a slight contraction of the transverse strain in three compositions, resulting in an increase of the unit cell volume ($\Delta V = S_{33} + 2S_{11}$). However, it can be seen that the transition from ferroelectric orthorhombic phase and ferroelectric rhombohedral phase at zero field to the field induced new ferroelectric phase involves no notable volume change in the case of x = 0.07 and x = 0.10 samples, respectively. The ΔV values in x = 0.07 and 0.10 samples are only ~0.09% and ~0.07%, respectively. By comparison, the ΔV value of the x = 0.05 sample is as high as ~0.27% at 10 kV/mm. This difference among different compositions should be attributed to the fact that the x = 0.05 sample exhibits the field induced antiferroelectric-ferroelectric phase transition, whereas the x = 0.07 and 0.10 samples own the field induced ferroelectric-ferroelectric phase transition. The volume train contribution along the field direction can be roughly estimated by using the relation $S_V = \Delta V/3$. The calculated

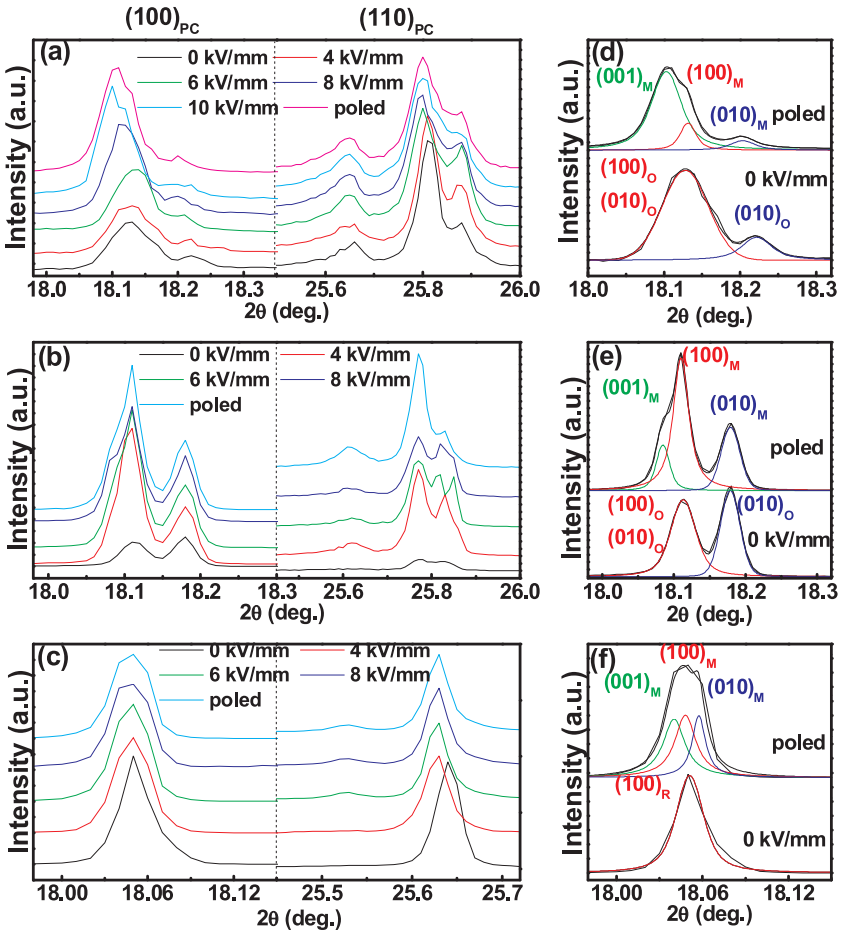

Fig. 7. The synchrotron XRD results of the (100) and (110) pseudo-cubic reflections at virgin, poling and poled states for with samples (a) x = 0.05, (b) x = 0.07, and (c) x = 0.10 samples, and the variation of (100) pseudo-cubic reflections at virgin (0 kV/mm) and poled states fitted by a pseudo-Voigt function for samples with (d) x = 0.05, (e) x = 0.07, and (f) x = 0.10 samples.

volume strain of the x = 0.05 sample is roughly 0.09%, while the volume strain of x = 0.07 and 0.10 samples are only 0.03% and 0.023%. It should be noted that the transverse strain is negative even at x = 0.05. This phenomenon is much different from that observed in typical $PbZrO_3$-based antiferroelectric ceramics, in which the positive transverse strain can be observed. The latter should be attributed to the specific relationship between lattice parameters of antiferroelectric tetragonal phases and ferroelectric rhombohedral phases.

The in-situ electric field synchrotron XRD results of some characteristic reflections for a few selected compositions are shown in Fig. 7. It should be noted that in the present study, the reflection lines were indexed by transforming the antiferroelectric orthorhombic P phase (Z = 8), ferroelectric orthorhombic Q phase (Z = 4) and ferroelectric rhombohedral phase (Z = 6) into the pseudo-cubic primitive cell in each composition, which can facilitate the lattice strain calculation. As shown in Fig. 7(a), the x = 0.05 sample shows a typical (100) doublet and a (110) triplet. Both peak positions and intensities show no obvious change as E ≤ 6 kV/mm, meaning that no polar axis aligns along the electric field direction (i.e., domain switching) and no elongation of the unit cell along the electric field (lattice strain) occurs in the above electric field range. However, with further increasing the field amplitude up to 8 kV/mm, additional reflections corresponding to the monoclinic symmetry starts to be detected in both (100) and (110) reflections. A further increase in the electric fields would cause a rapid increase of these peak intensities, meaning that the domain switching occurs only after the field induced monoclinic phase appears. In addition, it can be found that field induced monoclinic symmetry can be detected even after removal of the electric field, confirming that the phase transition is irreversible. This might be the reason why the poling strain S2 in the second cycle shows a good agreement with the S2' in the negative field side of the first cycle. Similar phase structure transition and domain switching behavior can be also observed in x = 0.07 and 0.10 samples (see Fig. 7(b, c)), although the virgin phase structures are different between these three compositions. To quantitatively calculate the lattice strain, the (100) reflections were fitted by a pseudo-Voigt function, as shown in Fig. 7(d–f). It should be noted that only $(001)_M$ reflection was considered for poled samples in the present study instead of all three peaks, and thus the calculated strain values should slightly deviate from the all irreversible lattice strain values. Actually, the strain contribution from the other reflections is relatively small, and thus the lattice strain calculations based on the $(001)_M$ reflection can be generally reliable. As a result, the calculated lattice strain S_L represents the irreversible lattice elongation along the electric field direction between virgin and poled samples, as calculated using the equation as follows:

$$S_L = \frac{d_{(001)_M} - d_{(001)_{O/R}}}{d_{(001)_{O/R}}} \times 100\% \quad (1)$$

where $d_{(001)_M}$ and $d_{(001)_{O/R}}$ represent 001_M lattice spacing and 001_O (or 001_R) lattice spacing at the poled and virgin states, respectively, as shown in Fig. 8. It is obvious that S_L value as high as ~0.165% was observed at x = 0.05. This value is much larger than those of the x = 0.07 (~0.12%) and 0.10 (~0.03%) samples. The high S_L and S_V should contribute to the observed large S_{irr} in the x = 0.05 sample. Fig. 8 also compares the calculated irreversible strain $S_{irr\text{-}cal}$ (= S_L + S_V) with the observed S_{irr}. It can be seen that $S_{irr\text{-}cal}$ in these three compositions keeps good agreement with S_{irr}. Most interestingly, the x = 0.05 sample exhibits not only a high lattice strain but also a high volume strain owing to the electric field induced irreversible antiferroelectric orthorhombic-ferroelectric monoclinic phase transition. This should be a general mechanism for the x ≤ 0.05 samples since these compositions exhibit similar antiferroelectric phase structures at

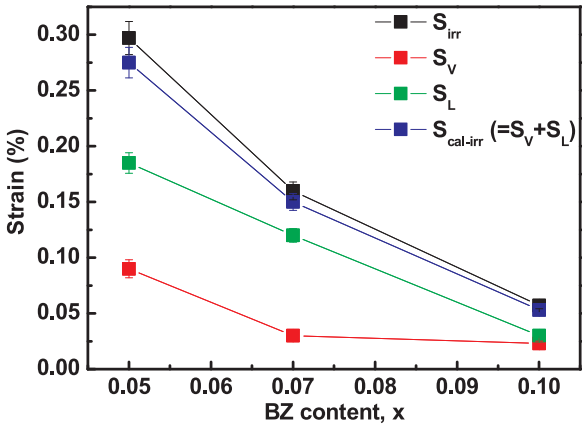

Fig. 8. The variation of S_{irr} observed in bipolar S-E curves from Fig. 5, the calculated lattice strain S_L and volume strain S_V and the calculated irreversible strain $S_{irr-cal}$.

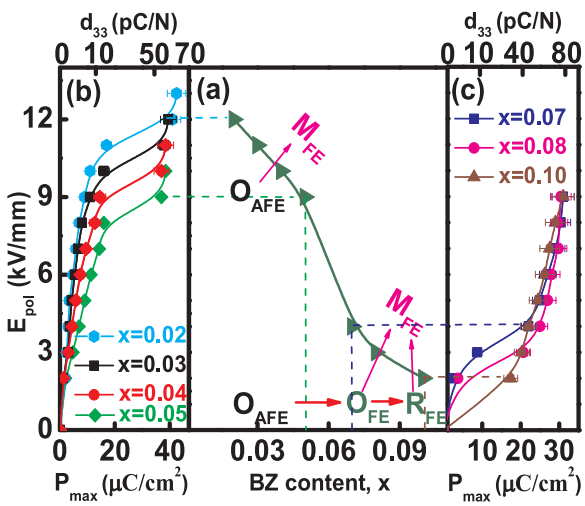

Fig. 9. (a) The composition-electric field phase diagram of (1-x)NN-xBZ ceramics, and (b and c) the saturated polarization P_{max} and quasi-static d_{33} as a function of poling field E_{pol} for various (1-x)NN-xBZ ceramics.

the virgin state and similar strain responses under electric field loading, obviously compared with x > 0.06 samples with orthorhombic and rhombohedral ferroelectric states at room temperature.

Fig. 9(a) shows the composition-electric field phase diagram of NN-xBZ system. It can be seen that the initial antiferroelectric or ferroelectric phase cannot be detected any more after poling. Instead, the ferroelectric monoclinic phase can be seen in the whole composition range after a high electric field was exerted, no matter what its virgin phase structure is. However, it can be seen from the Fig. 9(b) that the critical driving electric field for inducing irreversible antiferroelectric-ferroelectric phase transition decreases monotonously with increasing x. The critical electric field shows an obvious drop near x = 0.07 (Fig. 9(c)), possibly due to relatively low critical field values required for the field-induced ferroelectric-ferroelectric phase transition. The field induced ferroelectric monoclinic phase exhibits a low piezoelectric response (d_{33} ~ 50–70 pC/N in Fig. 9(b,c)), further indicating a negligible piezoelectric lattice strain contribution in large poling strains.

4. Conclusions

The composition and electric field dependent phase structure transformation in lead-free (1-x)NN-xBZ solid solution ceramics was explored by means of the measurement of XRD data and the dielectric permittivity together with strain-electric field curves. The substitution of BZ for NN was found to induce a series of phase transitions from antiferroelectric orthorhombic P phase to ferroelectric orthorhombic Q phase transition and finally into ferroelectric rhombohedral phase. Most interestingly, ultrahigh poling strains of ~0.58% were found to be accompanied by an irreversible field-induced antiferroelectric to ferroelectric monoclinic phase transition in the composition range of 0.02 ≤ x ≤ 0.05, which involve a distinct volume expansion and an obvious lattice elongation along the field direction, accounting for 70–75% of the total poling strain. By comparison, the compositions with 0.06 ≤ x ≤ 0.11 in the ferroelectric orthorhombic or rhombohedral phase zone own much smaller poling strains but still asymmetric bipolar first-cycle strain curves owing to field induced irreversible ferroelectric orthorhombic or rhombohedral to ferroelectric monoclinic phase transition, as supported by the measurement of in-situ longitudinal and transverse strains and the quantitative analysis of in-situ synchrotron XRD data.

Acknowledgements

This work was supported by the National Natural Science Foundation of China (Grants No. 51472069, U1432113, 51402079).

References

[1] Y. Saito, H. Takao, T. Tani, T. Nonoyama, K. Takatori, T. Homma, T. Nagaya, M. Nakamura, Lead-free piezoceramics, Nature 432 (2004) 84–87.
[2] M. Matsubara, K. Kikuta, S. Hirano, Piezoelectric properties of (K0.5N0.5)(Nb1-xTax)O3-K5.4CuTa10O29 ceramics, J. Appl. Phys. 97 (2005) 114105.
[3] T.A. Skidmore, T.P. Comyn, S.J. Milne, Temperature stability of ([Na0.5K0.5NbO3]0.93-[LiTaO3]0.07) lead-free piezoelectric ceramics, Appl. Phys. Lett. 94 (2009) 222902.
[4] J. Fu, R.Z. Zuo, H. Qi, C. Zhang, J.F. Li, L.T. Li, Low electric-field driven ultrahigh electrostrains in Sb-substituted (Na,K)NbO3 lead-free ferroelectric ceramics, Appl. Phys. Lett. 105 (2014) 242903.
[5] J. Koruza, P. Groszewicz, H. Breitzke, G. Buntkowsky, T. Rojac, B. Mali, Grain-size-induced ferroelectricity in NaNbO3, Acta Mater. 126 (2017) 77–85.
[6] L.A. Reznitchenko, A.V. Turik, E.M. Kuznetsova, V.P. Sakhnenko, Piezoelectricity in NaNbO3 ceramics, J. Phys.: Condens. Matter 13 (2001) 3875–3881.
[7] M. Tyunina, A. Dejneka, D. Rytz, I. Gregora, F. Borodavka, M. Vondracek, J. Honolka, Ferroelectricity in antiferroelectric NaNbO3 crystal, J. Phys.: Condens. Matter 26 (2014) 125901.
[8] J. Frederick, X.L. Tan, Strains and polarization during antiferroelectric-ferroelectric phase switching in Pb0.99Nb0.02[(Zr0.57Sn0.43)1-yTiy]0.98O3 ceramics, J. Am. Ceram. Soc. 94 (2011) 1149–1155.
[9] A.M. Glazer, H.D. Megaw, Studies of the lattice parameters and domains in the phase transitions of NaNbO3, Acta Cryst. A 29 (1973) 489–495.
[10] Y.H. Xu, W. Hong, Y.J. Feng, X.L. Tan, Antiferroelectricity induced by electric field in NaNbO3-based lead-free ceramics, Appl. Phys. Lett. 104 (2014) 052903.
[11] L. Chao, Y.D. Hou, M.P. Zheng, M.K. Zhu, High dense structure boosts stability of antiferroelectric phase of NaNbO3 polycrystalline ceramics, Appl. Phys. Lett. 108 (2016) 212902.
[12] K.E. Johnston, C.C. Tang, J.E. Parker, K.S. Knight, P. Lightfoot, S.E. Ashbrook, The polar phase of NaNbO3: a combined study by powder diffraction, solid-state NMR, and first-principles calculations, J. Am. Chem. Soc. 132 (2010) 8732–8746.
[13] P. Vousden, The structure of ferroelectric sodium niobate at room temperature, Acta Crystallogr. 4 (6) (1951) 545–551.
[14] L.A. Reznichenko, L.A. Shilkina, E.S. Gagarina, I.P. Raevskii, E.A. Dul'kin, E.M. Kuznetsova, V.V. Akhnazarova, Structural instabilities, incommensurate modulations and P and Q phases in sodium niobate in the temperature range 300-500 K, Crystallogr. Rep. 48 (2003) 448.
[15] S. Yamazoe, A. Kohori, H. Sakurai, Y. Kitanaka, Y. Noguchi, M. Miyayama, T. Wada, Laser beam scanning microscope and piezoresponse force microscope studies on domain structured in 001-, 110-, and 111-oriented NaNbO3 films, J. Appl. Phys. 112 (2012) 052007.
[16] I. Lefkowitz, K. Lukaszewicz, H.D. Megaw, The high-temperature phases of sodium niobate and the nature of transitions in pseudosymmetric structures, Acta Crystallogr. 20 (5) (1966) 670–683.
[17] H. Shimizu, H.Z. Guo, S.E. Reyes-Lillo, Y. Mizuno, K.M. Rabe, C.A. Randall, Lead-free antiferroelectric: xCaZrO3-(1-x)NaNbO3 system (0 ≤ x ≤ 0.10), Dalton Trans. 44 (2015) 10763–10772.
[18] H.Z. Guo, H. Shimizu, Y. Mizuno, C.A. Randall, Strategy for stabilization of the antiferroelectric phase (Pbma) over the metastable ferroelectric phase (P21ma) to establish double loop hysteresis in lead-free (1-x)NaNbO3-xSrZrO3 solid solution, J. Appl. Phys. 117 (2015) 214103.
[19] L.S. Gao, H.Z. Guo, S.J. Zhang, C.A. Randall, A perovskite lead-free antiferroelectric xCaHfO3-(1-x)NaNbO3 with induced double hysteresis loops at room temperature, J. Appl. Phys. 120 (2016) 204102.
[20] D.S. Fu, T. Arioka, H. Taniguchi, T. Taniyama, M. Itoh, Ferroelectricity and electromechanical coupling in (1-x)AgNbO3-xNaNbO3 solid solutions, Appl. Phys. Lett. 99 (2011) 012904.

[21] R.D. Shannon, Revised effective ionic radii and systematic studies of interatomic distances in halides and chalcogenides, Acta Cryst. A 32 (1976) 751.
[22] A.M. Glazer, Simple ways of determining perovskite structure, Acta Crystallogr. A 31 (1975) 756–762.
[23] Yu.I. Yuzyuk, E. Gagarina, P. Simon, L.A. Reznitchenko, L. Hennet, D. Thiaudiere, Synchrotron x-ray diffraction and Raman scattering investigations of (LixNa1-x) NbO3 solid solutions: evidence of the rhombohedral phase, Phys. Rev. B 69 (2004) 144105.
[24] X.L. Tan, C. Ma, J. Frederick, S. Beckman, K.G. Webber, The antiferroelectric ↔ ferroelectric phase transition in lead-containing and lead-free perovskite ceramics, J. Am. Ceram. Soc. 94 (2011) 4091–4107.
[25] S.K. Mishra, R. Mittal, V.Yu. Pomjakushin, S.L. Chaplot, Phase stability and structural temperature dependence in sodium niobate: a high-resolution powder neutron diffraction study, Phys. Rev. B 83 (2011) 134105.